Chapter 7

Anhydrous NiC_2O_4 Quantum dots(QDs): A superior pseudocapacitive electrode for large-scale energy storage applications in aqueous KOH and neutral Na_2SO_4 electrolyte

7.1 Introduction

Demand for bulk energy storage and distribution for a variety of portable electronics and automobiles is continuously increasing. Further to utilize the full potential of renewable energy sources such as wind turbines and photovoltaics, the development of grid-scale energy storage and transmission solutions is mandatory. Electrochemical energy storage is the most successful way to store and deliver renewable power due to the high theoretical efficiency of converting chemicals to electrical energy coupled with the high energy densities and power densities achieved in rechargeable batteries.[1-3] The energy storage process of electrode surfaces is a complex phenomenon due to the interaction of electrodes with electrolytes. Generally, three types of interaction namely EDLC, surface redox, and intercalation of ions occur on the electrode surface between electrode and electrolyte.[4-5]

The first redox-mediated charge storage type pseudocapacitance behaviour was observed in reported materials first RuO_2.[6] According to the charge storage mechanism, pseudocapacitors denote accessibility to different oxidation states for redox charge transfer and can achieve higher energy density compared to EDLC.[7-9] Metal-organic frameworks (MOFs) as interesting open pore structures where materials are constructed by joining metal-containing units with organic linkers, using strong bonds with permanent porosity.[10-12] Highly porous metal oxalate shows faradaic pseudocapacitive characteristics coupled with reversible redox reaction mechanism observed over active transition metal ion having the accessibility of multiple oxidation states. [13-16.]

The quantum dots (QDs) are a special class of nanomaterials (particle size in the range of 2−10 nm in diameters) that show quantum confinement effects coupled with

accelerating the excellent physical and chemical diffusion and catalytic activities.[17-18] Quantum dots (QDs) structure of the active material of the electrode is known to display very attractive applications in energy storage. The ultra-small size of QDs empowers the active materials with a larger specific surface area (larger surface-to-volume ratio) loading and prosperous maximum active sites that make the redox and conversion reaction of the electrode more efficient. The highly porous structure inside the QDs provided a short ion diffusion pathway, allowing ions to smoothly penetrate and participate in the electrochemical reaction. Consequently, the reaction is expected to transform from diffusion control to surface control, and the charge transfer occurs more rapidly. [19-21]

In this work, we present the synthesis, characterization, and electrochemical energy storage performances of both $NiC_2O_4.2H_2O$ QDs and anhydrous NiC_2O_4 QDs. The specific capacitance value equivalent to 1638 F/g at 1A/g was obtained for anhydrous NiC_2O_4 QDs and hydrated $NiC_2O_4.2H_2O$ QDs showed a superior capacitance equivalent to 1150 F/g at 1A/g in aqueous 2M KOH electrolyte. Further, electrodes were assembled in aqueous asymmetric supercapacitors (ASCs) mode in which porous anhydrous NiC_2O_4 QDs are made as the positive electrode and Activated Carbon (AC) as the negative electrode resulting specific energy capacity equivalent to 293 Wh/kg and specific power of ~772W/kg at 1 A/g current density.

7.2 Material Synthesis and Characterizations:

Anhydrous porous NiC_2O_4 QDs were synthesized in a two-step process using a controlled precipitation method followed by slow heating of precipitates 1:1 ratio of H_2O and isopropyl alcohol solution was used as a solvent in the preparation of quantum dots. **Figure7.1** shows the schematic representation of the synthesis process. 0.5 millimoles (mM) of Nickel(II) nitrate hexahydrate ($Ni(NO_3)_2.6H_2O$) and 0.5 millimoles (mM) oxalic acid dehydrate ($H_2C_2O_4.2H_2O$) were dissolved separately in 50 ml of double-distilled water and both solutions were filled separately in the burettes. As shown in **Figure7.** 1, solutions were added dropwise with continuous stirring in three necks conical in a flask containing 200ml of 1:1 ration of H_2O and isopropyl alcohol solution and placed at a hot plate magnetic stirrer. The entire mixture was stirred vigorously at 80^oC for 2h. Then the dilute colloidal reactant

product $NiC_2O_4.2H_2O$ QDs were separated by centrifuged technic and washed several times with ethanol. Finally, the washed product $NiC_2O_4.2H_2O$ was dried in a vacuum dry oven at 80^o overnight. Anhydrous highly porous NiC_2O_4 QDs were formed after calcination of $NiC_2O_4.2H_2O$ ODs at 180^oC for 5h in a hot vacuum air oven. The reaction of the formation of NiC_2O_4 QDs is presented in **equations 7.1& 7.2** given below.

$$Ni(NO_3)_2.6H_2O + H_2C_2O_4.2H_2O \rightarrow NiC_2O_4.2H_2O\downarrow + 2HNO_3 + 2H_2O \quad \text{at} \quad 80^oC \qquad (7.1).$$

$$NiC_2O_4.2H_2O \longrightarrow NiCO_4 + 2H_2O\uparrow \qquad \text{at } 180^oC \qquad (7.2)$$

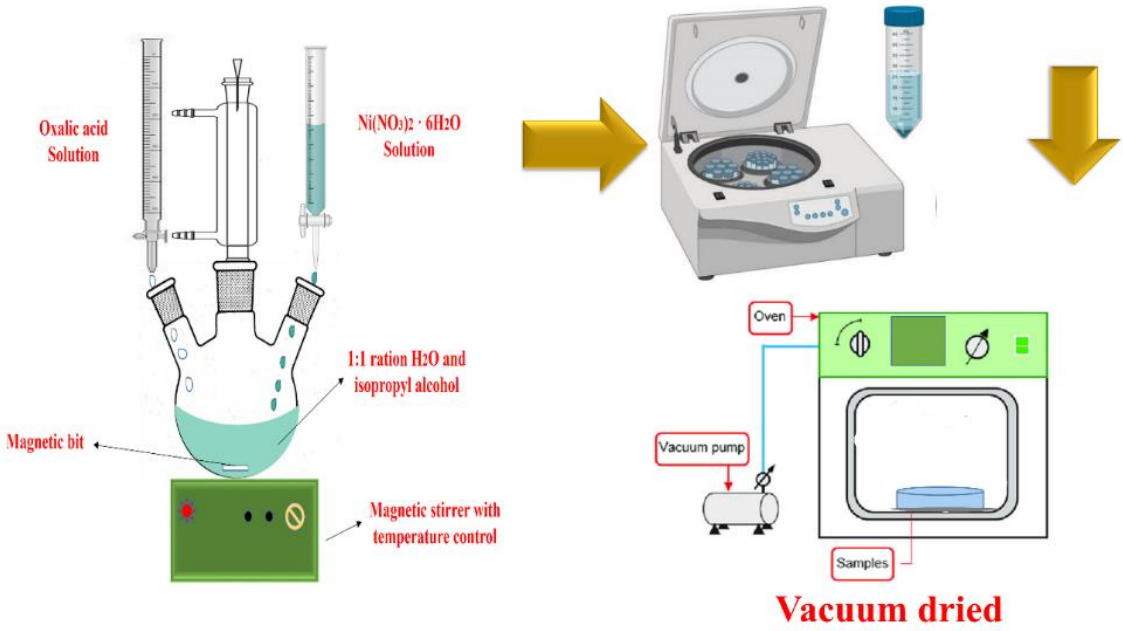

Figure 7. 1. Schematic representation of synthesis process of $NiC_2O_4.2H_2O$ and anhydrous NiC_2O_4 quantum dots (QDs).

The crystal structure and phase purity of synthesized products were characterized through RigakuMiniflex desktop X-ray Diffractometer (XRD) with Cu-Ka radiation (λ= 0.154nm) in the range 2θ=10º–90º with a step size of 0.02º. Xpert High Score (PANanylytical) software was used to identify the phase/structure of the samples. The structures were refined by the Rietveld refinement method using the FULLPROF

suite software package and monoclinic $NiC_2O_4.2H_2O$ (space group: Cccm) and Monoclinic NiC_2O_4 (space group: P21/n) as model structure. FE-SEM (FP 5022/22) was used to determine the surface structure and morphology of the sample. Infrared spectra of the samples were recorded using a Nicolet iS5 FTIR spectrometer in the range of 400 to 4000 cm-1. Pore size distribution and specific surface area of the sample were measured by BET (MicrotracBEL). X-ray Photo-electron Spectroscopy (XPS) studies were carried out to investigate the electronic structures of the materials. XPS of the sample was carried out by Thermo Scientific Multilab 2000 instrument using Al Kα radiation operated at 150W. Binding energies reported here are concerning C (1s) at 284.5 eV and they are accurate within ±0.1 eV. All electrochemical performances of the sample including cyclic voltammetry (CV), galvanostatic charge-discharge (GCD), and Electrochemical impedance spectroscopy (EIS) were conducted using a conventional three-electrode arrangement and were measured by Metrohm Autolab (PGSTAT204) equipped with a FRA32M module. Electrochemical measurements were analyzed using NOVA1.1 software.

7.2.1 Preparation of Electrode:

Working electrodes of $NiC_2O_4.2H_2O$ QDs and anhydrous NiC_2O_4 QDs were prepared by taking active material, activated carbon, and binder (PVDF) in NMP solvent in the ratio of 7:2:1. The homogenous slurry was prepared in mortar and slurry containing ~1mg active materials were cast over $1cm^2$ area of Toray carbon paper. The coated electrode was dried at 80^oC for 12hrs. The electrode loading was calculated by taking the weight of the electrode through electronic balance (error limit: 0.01mg). For that, the weight of Torrey paper was taken first, and then the weight of coated electrode (after drying the coated ink on Torrey carbon paper on a $1x1cm^2$ area was taken for the study. Then from the difference in the weight, the exact loading of electrode material was calculated.

7.3 Results and Discussions:

7.3.1 Crystallographic characterization

Figure.7.2 (a)shows Rietveld refined XRD profile of $NiC_2O_4.2H_2O$ QDs over the range of 2θ range of 10-60° with step size 0.02 º. The diffraction peaks appeared at 18.86, 22.68, 30.38, 35.8, and 47.1° in the black curve, matching very well to the (202), (004), (400), (022), and (206) planes of $NiC_2O_4{\cdot}2H_2O$ QDs (JCPDS No. 25-

0582, monoclinic structure, Space group: Cccm, lattice parameters a=11.77800,b= 5.19600 c= 15.62800). The sharp peaks that appeared in the powder XRD profile confirm the good crystallinity of the QDs.[22]

Figure 7.2 (b) shows the Rietveld refined XRD profile of anhydrous NiC_2O_4QDs ($NiC_2O_4.2H_2O$ sample annealed at 180^oC for 5hrs). The structure of NiC_2O_4 QDs is assigned to an α-monoclinic structure. The XRD peaks at 23.56, and 37.61 corresponds to (110), (210) plane of α-monoclinic structure (space group P21/n, JCPDS no. 37-0719). [23]

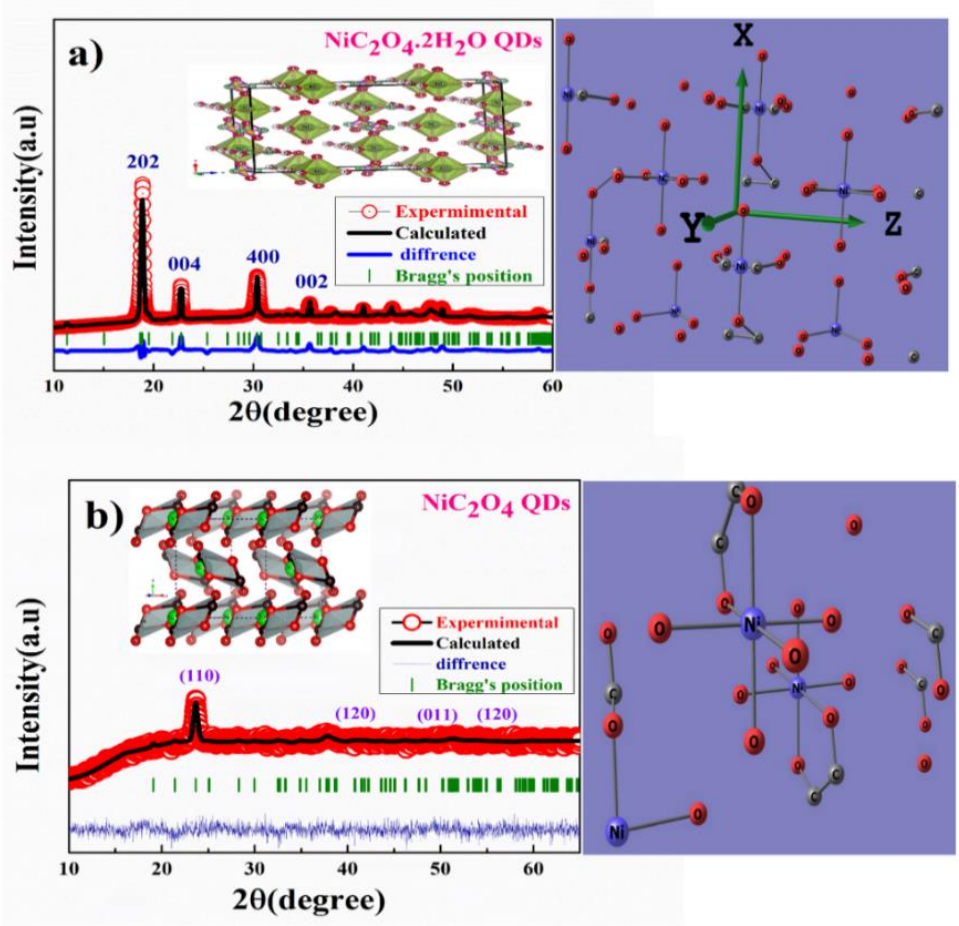

Figure 7.2. (a) xrd pattern of $NiC_2O_4.2H_2O$ QDs (b) anhydrous NiC_2O_4 QDs

7.3.2 Thermo-gravimetric Analysis (TGA) and Differential thermal analysis (DTA)

A comparative Thermo-gravimetric analysis (TGA) study of $NiC_2O_4.2H_2O$ QDs and bulk NiC_2O_4 $.2H_2O$ is shown in **Figure7.3** First weight loss occurred in the temperature ranges of 100ºC-300ºC for QDs and bulk of $NiC_2O_4.2H_2O$, which corresponds to the removal of structural water from the sample and the formation of an anhydrous phase occurs. DTA plot is shown in the inset of Fig. 2c. The water removal step starts at around 174^{o}C for $NiC_2O_4.2H_2O$ QDs compared to bulk $NiC_2O_4.2H_2O$ where water removal starts at around 217^{o}C temperature. The first weight loss was 28% suggesting two moles of water got removed from the sample between temperature ranges of 100ºC-300ºC. That is why we carried out annealing for water removal at 180 ^{o}C to prepare anhydrous NiC_2O_4QDs. Similarly, the second weight loss step corresponds to 36 % weight loss occurring in the temperature range of 350–500ºC due to the decomposition of NiC_2O_4 QDs and bulk. QDs decomposition starts at a lower temperature compared to bulk materials. The weight losses for QDs are represented in **equations 3 and 4**.

$$NiC_2O_4.2H_2O\ QDs \rightarrow NiC_2O_4\ QDs + 2H_2O \quad (T \geq 170\ ^oC \qquad (7.3)$$

$$NiC_2O_4\ QDs \rightarrow \quad NiO + 2CO_2 \quad (T \geq 350^oC) \qquad (7.4)$$

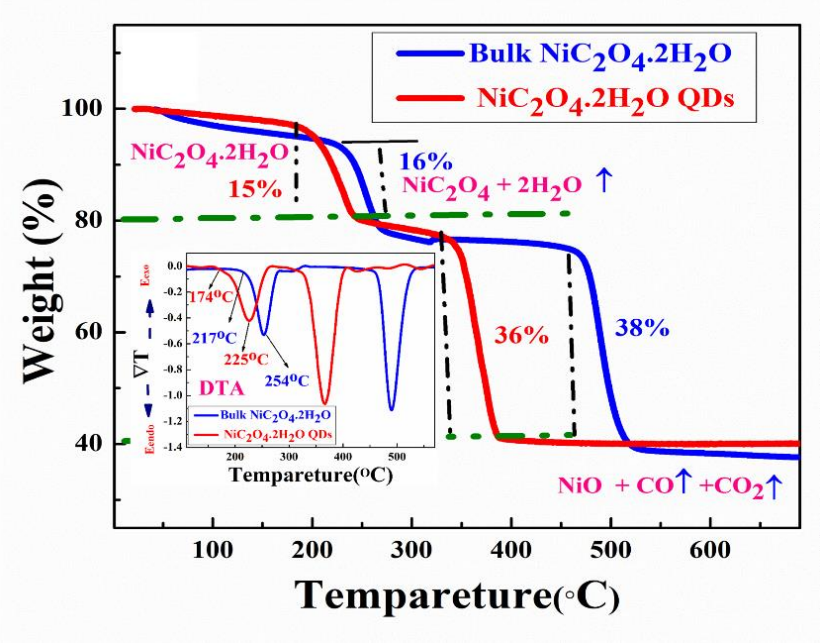

Figure 7.3 TGA and DTA of bulk $NiC_2O_4.2H_2O$ and $NiC_2O_4.2H_2O$ QDs sample

7.3.3 Fourier transform infrared spectroscopy (FTIR) analysis

FT-IR spectrums of $NiC_2O_4.2H_2O$ QDs and anhydrous NiC_2O_4 QDs powder samples are shown in **Figure7.4** revealing the presence of different functional groups at different wavenumber (cm^{-1}). The broad peak at 3404.35 cm^{-1} ascribed to the stretching vibration of a hydroxyl group (-OH) signifies the presence of water in the compound. The observed peak at 1604.45 cm^{-1} was assigned for the anti-symmetric carbonyl stretching band (C=O) specific to the oxalate group.[20] Other peaks at 1361.86 cm^{-1} and 1316.75 cm^{-1} were attributed to vibrations of $C_2O_4^{-2}$ (C–O) + (C–C) and (C–O) + (O–C=O), respectively. The peak at 843.16 cm^{-1} was assigned to the vibration mode of $C_2O_4^{-2}$(O–C=O bending vibrations). The absorption peak at 488.43 cm^{-1} can be attributed to the combining Ni-O bonds present in a prepared sample of $NiC_2O_4.2H_2O$ QDs as it appears at 543.97 cm^{-1} in NiC_2O_4 QDs. The stretching vibration of the hydroxyl group (-OH) near 3372.73 cm^{-1} peak intensity was reduced severely in the case of NiC_2O_4 QDs suggesting the removal of almost all H_2O molecules from the structure. [24]

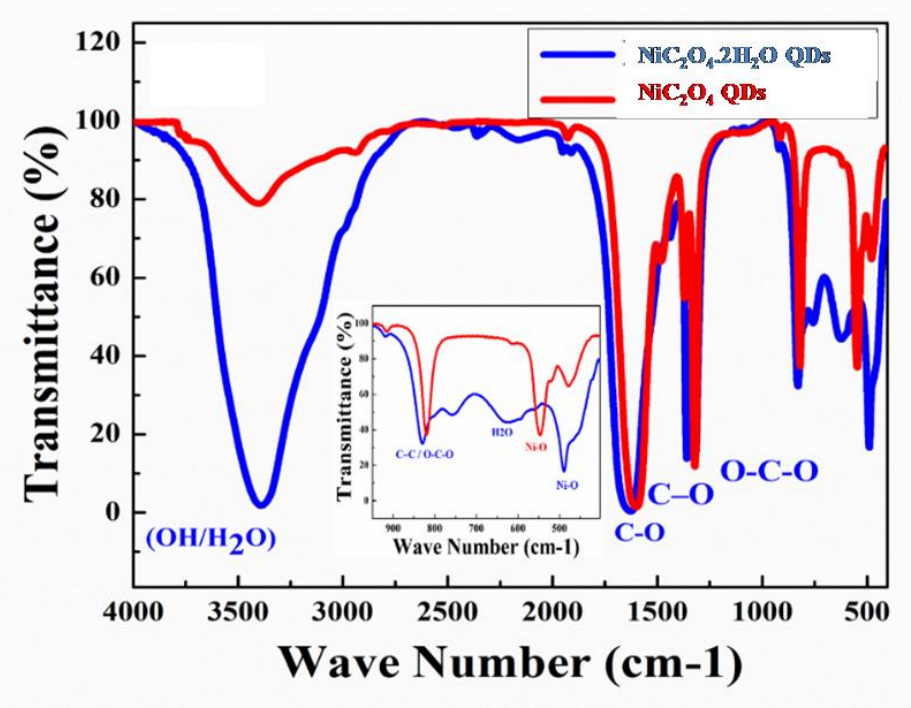

Figure 7.4 FT-IR spectrums of $NiC_2O_4.2H_2O$ QDs and anhydrous NiC_2O_4 QDs powder samples

7.3.4 Brunauer-Emmett-Teller (BET) surface area analysis

Figure 7.5 shows a comparative Brunauer-Emmett-Teller (BET) surface area measurement plots of $NiC_2O_4.2H_2O$ QDs and NiC_2O_4 QDs. The nitrogen adsorption and desorption isotherm show characteristics that correspond to the mesoporous structure for the NiC_2O_4 QDs sample. The calculated BET-specific surface areas were found to be 133 and 216.38 m^2/g respectively of $NiC_2O_4.2H_2O$ QDs and NiC_2O_4 QDs samples. The pore size distribution curves shown in the insert indicate the presence of mesopores with pore sizes ranging from 5 to 7 nm and 11 to 16 nm respectively. Mesoporous structures provide fast-ion transport channels and the high electrostatic adsorption capacity of microspores resulting in excellent electrochemical energy storage activity. The calculated mesopores diameter of the NiC_2O_4 QDs sample is much bigger than the ions present in aqueous electrolytes. [25-26]

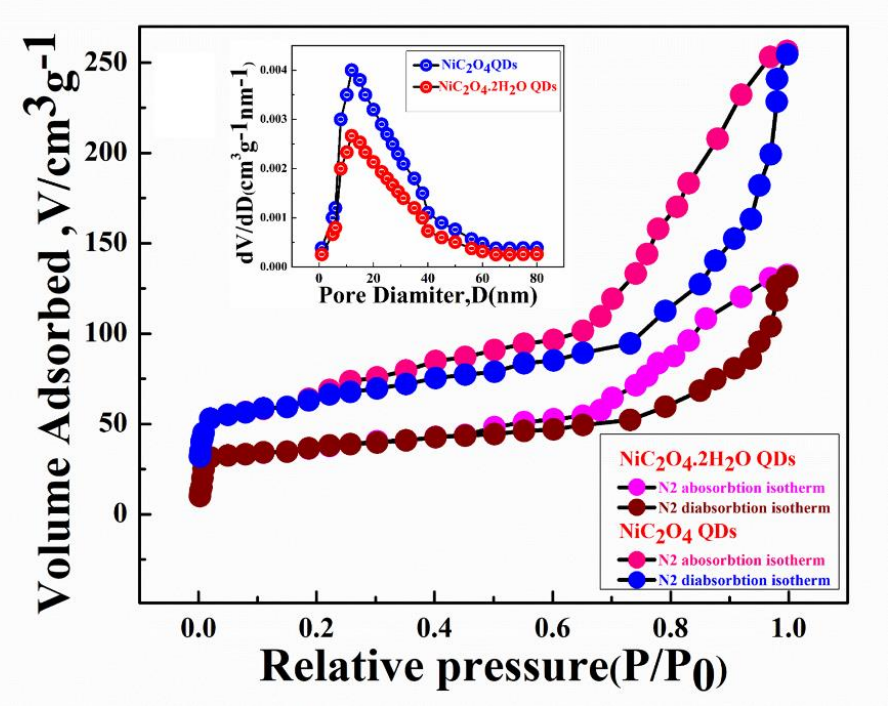

Figure 7.5 BET surface area measurements plot of $NiC_2O_4.2H_2O$ QDs and NiC_2O_4 QDs

7.3.5 Raman spectrum analysis

A comparative FT-Raman study of $NiC_2O_4.2H_2O$ QDs and anhydrous NiC_2O_4 QDs was carried out and presented in **Figure 7.6**. One-phonon longitudinal optical (LO) mode was observed both in $NiC_2O_4.2H_2O$ QDs and anhydrous NiC_2O_4 QDs in different frequency regions. LO mode was observed in $NiC_2O_4.2H_2O$ QDs at 538 cm^{-1} and 595 cm^{-1} and in the case of anhydrous NiC_2O_4 QDs LO mode was observed at 547 cm^{-1} and 607 cm^{-1}. The combined one-phonon longitudinal and one-phonon optical (LO + TO) mode was observed at 921 cm^{-1} for both $NiC_2O_4.2H_2O$ QDs and anhydrous NiC_2O_4 QDs [27] The doublet peak consisting of a low-intensity shoulder peak at 1451 and a high-intensity peak at 1477 cm^{-1} are associated with a two-magnon (2 M) band that arises from the Ni^{2+}- O^{2-}- Ni^{2+} vibration confirming the existence of hydrated nickel oxalate phase, whereas only single peak was observed for anhydrous NiC_2O_4 QDs at 1484 cm^{-1}.

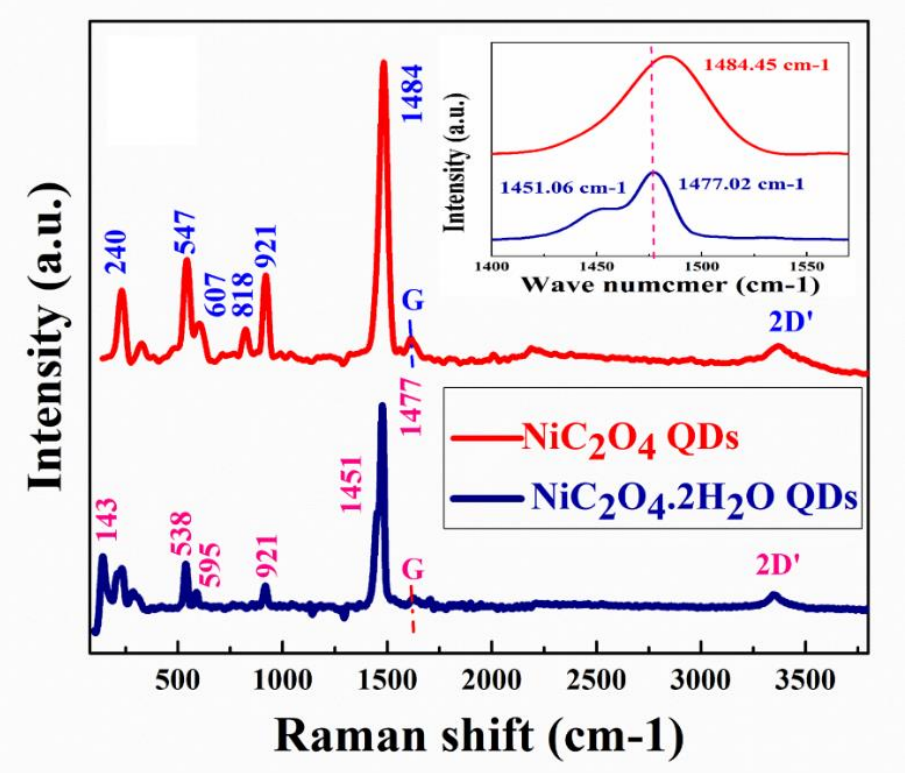

Figure 7.6 Raman shift of $NiC_2O_4.2H_2O$ QDs and NiC_2O_4 QDs

The Raman bands were observed both at 1626 and 1614 cm^{-1} for $NiC_2O_4.2H_2O$ QDs and anhydrous NiC_2O_4 QDs respectively and they correspond to the G band that arises due to the C-C bond stretching vibration in the graphitic plane. Symmetrical

stretching in the carboxylic functional group second-order disorder peaks 2D' appeared at 3345.29 cm^{-1} and 3363.51 cm^{-1} respectively in $NiC_2O_4.2H_2O$ QDs and anhydrous NiC_2O_4 QDs samples. Thus FT-Raman study confirms the effective formation of anhydrous NiC_2O_4 QDs. [27-28]

7.3.6 UV visible spectroscopy analysis

Figure 7.7 (a) shows a comparative UV absorbance curve of both bulk and QD of anhydrous NiC_2O_4. Anhydrous NiC_2O_4 QDs show an absorbance peak at the 241nm wavelength region whereas the bulk NiC_2O_4 shows an absorbance peak at 342 nm wavelength. **Figure 7.7 (b)** represents the Tauc plot to determine the bandgap of both bulk and QDs of anhydrous NiC_2O_4. in general, the QDs band gap is higher compared to bulk materials due to quantum confinement. The bandgap of bulk and QDs of anhydrous NiC_2O_4 were found to be 3.61 eV and 5.14 eV respectively.

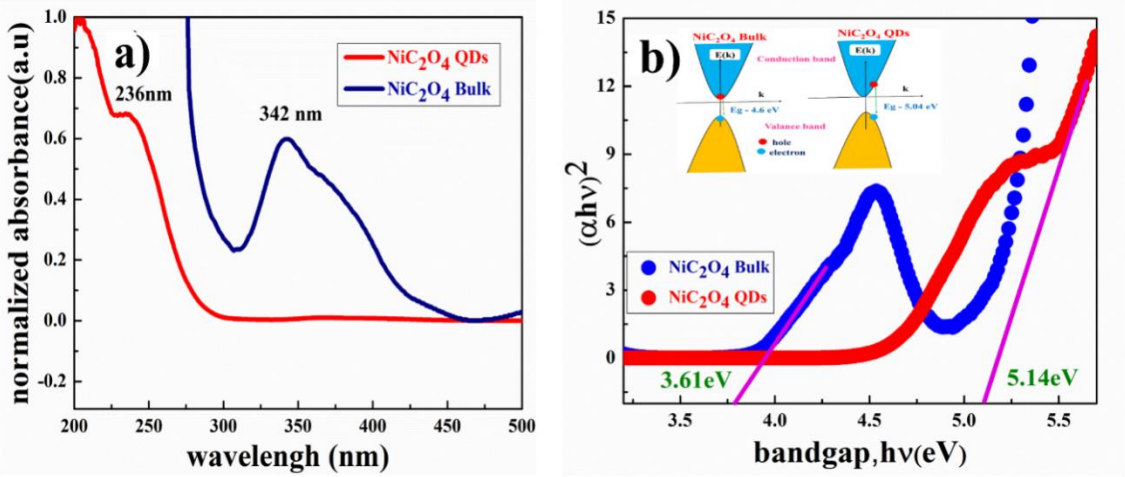

Figure 7.7 a) UV absorbance of bulk and NiC_2O_4 QDs sample (b) bandgap of bulk and NiC_2O_4 QDs

7.3.7 X-ray photoelectron spectroscopy (XPS) analysis

Figure 7.8 (a) shows X-ray photoelectron spectroscopy (XPS) characterization was carried out to determine the variations of chemical composition and the confirmation of functional groups in the resultant NiC_2O_4 QDs. Further confirming the presence of Ni in composition, The Ni2p spectrum shown in **Figure 7.8 (b)** could be divided into

peaks, which are assigned to $2p_{3/2}$ of Ni^{2+} (856.46 eV) ion and $2p_{1/2}$ of Ni^{2+} (874.37 eV) ions, as well as the corresponding satellite peaks at 861.94 eV and 880.03 eV. The C1s spectrum is shown in

Figure 7.8 (c) 284.43 eV corresponding to C-C/C=C and C-O, C=O bond stretching at 285.43 eV 288.59eV respectively. The O1s spectrum shown in **Figure 7.8 (d)** represents C=O and C-O bond stretching at 530.23eV and 528.58eV. [30-31]

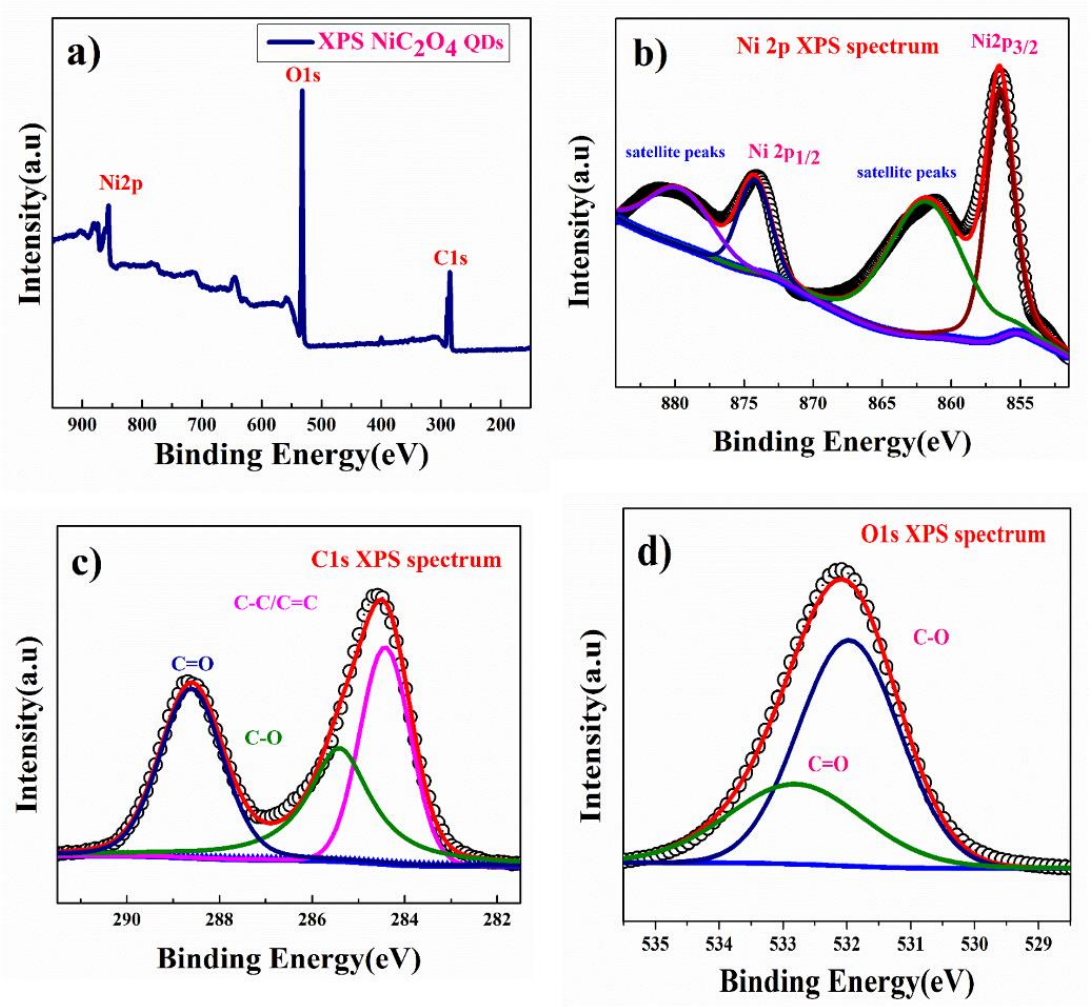

Figure 7.8 XPS plot of (a) full survey NiC_2O_4 QDs (b) Ni (2p) spectrum and (c) Co 2p spectrum (d) O (1s) spectrum

7.3.8 High-resolution scanning electron microscopy (HRSEM) analysis

HRSEM image shown in **Figure 7.9 (a-b)** displays the morphology of $NiC_2O_4.2H_2O$ QDs and NiC_2O_4 QDs. Both $NiC_2O_4.2H_2O$ QDs and NiC_2O_4 QDs particles pose a Nanoplates type arrangement. **Figure 7.9 (c)** shows the (Energy Dispersive X-ray Analysis) result of anhydrous NiC_2O_4QDs confirming the elemental composition of the material. **Figure 7.9 (d-f)** shows an image mapping of the anhydrous NiC_2O_4 QDs sample presenting the elements (Ni, C, and O) distribution in the material

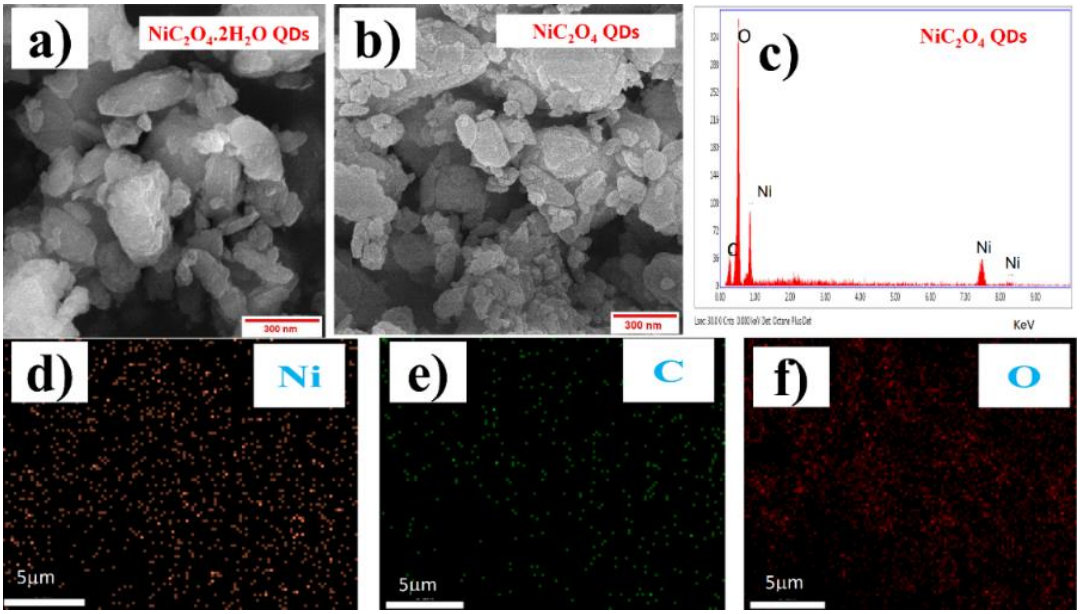

Figure 7.9 HRSEM image showing the morphology and particle size distribution of (a) $NiC_2O_4.2H_2O$ QDs (b) anhydrous NiC_2O_4 QDs, (c) EDX of anhydrous NiC_2O_4 QDs (d-f) elemental distribution of Ni, C, O of NiC_2O_4 QD

7.3.9 High-resolution scanning electron microscopy (HRSEM) analysis

TEM images of $NiC_2O_4.2H_2O$ QDs shown in **Figure 7.10 (a)** confirm the particle size distribution in the range of 4 to 8 nm (particle size was determined using **ImageJ** software). The inset image represents FFT (Fast Furrier Transformation) and inverse FFT of (202) plane of $NiC_2O_4.2H_2O$ QDs. **Figure 7.10 (b)** shows calculated d spacing equivalent to 0.489 nm of (202) plane $NiC_2O_4.2H_2O$ QDs using Gatan GMS3 software. **Figure 7.10 (c)** shows the particle distribution (3 to 5 nm) of anhydrous NiC_2O_4 QDs quantum dots determined by the **ImageJ** software. The inset image represents FFT (Fast Furrier Transformation) and inverse FFT of (101) plane of

anhydrous NiC_2O_4 QDs. **Figure 7.10 (d)** shows calculated d spacing equivalent to 0.347 nm of (110) plane of anhydrous NiC_2O_4 QDs.

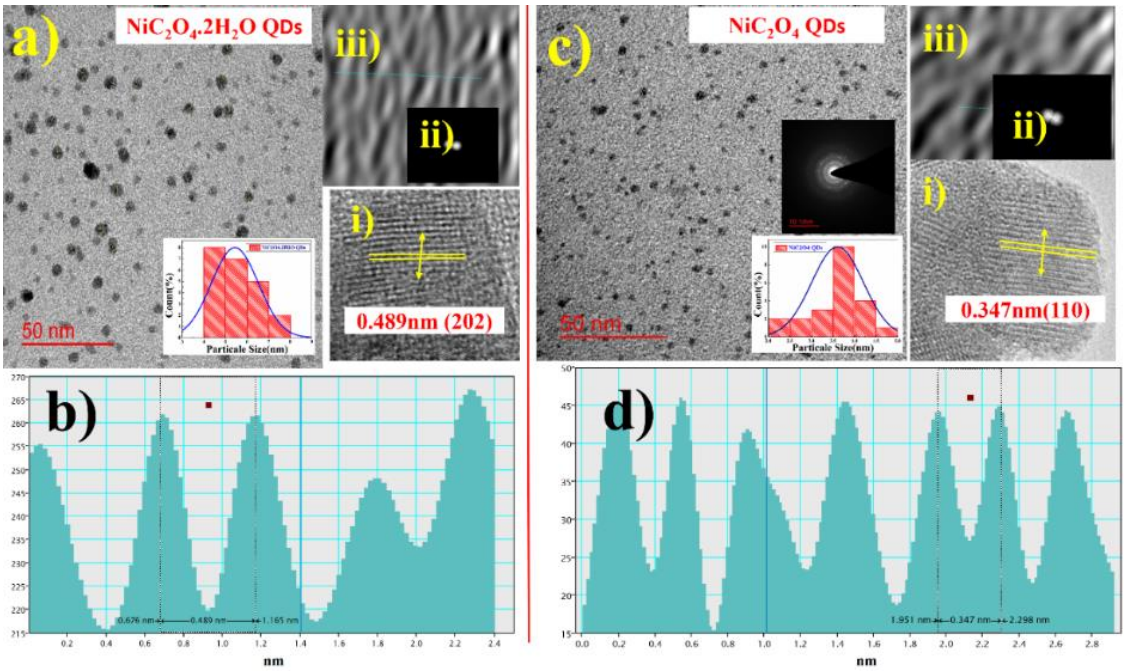

Figure 7.10 HRTEM image at localized regions showing QDs of (a) $NiC_2O_4.2H_2O$ QDs particle size with distribution (with FFT and inverse FFT) (b) calculating d-spacing of (202) plane (c) NiC_2O_4.QDs particle size with distribution (with FFT and inverse FFT) and (d) d-spacing of (110) plane.

7.3.10 Cyclic Voltammetry analysis

Electrochemical properties and performance of $NiC_2O_4.2H_2O$ QDs and anhydrous NiC_2O_4 QDs were measured using a three-electrode system where $NiC_2O_4.2H_2O$ QDs and porous anhydrous NiC_2O_4 QDs was used as working electrodes. In a three-electrode system, saturated Hg/HgO (1M KOH) as a reference electrode, and thick Platinum wire was utilized as a counter electrode in a 2M KOH electrolyte. The charge storage capacity of $NiC_2O_4.2H_2O$ QDs and anhydrous NiC_2O_4 QDs was examined using the Cyclic-voltammetry (CV) curve between the potential range of 0 V to 0.6 V. **Figure 7.11 (a -b)** represents the CV curve of $NiC_2O_4.2H_2O$ QDs and anhydrous NiC_2O_4 QDs. The nature of the curve represents the pseudocapacitive behaviour dominating both surface and diffusion-controlled redox (electrosorption). A good sharp CV curve with diffusion control dominating with surface control redox process obtains up to 200mV/s due to fast diffusion of ions QD structure. Redox peaks originated due to the reversible transformation between Ni^{2+} to Ni^{3+} through Electrosorption (redox) of OH^- ion.[32]

$$Ni(II)C_2O_4.2H_2O + OH^-_{sol} \longleftrightarrow Ni(III)(OH^-)C_2O_4.2H_2O + e^- \quad (7.5)$$

$$Ni(II)\ C_2O_4 + OH^-_{sol} \longleftrightarrow Ni\,(III)(OH^-)\,C_2O_4 + e^- \quad (7.6)$$

The specific capacitance C (F/g) was determined from the CV using the **equation.7.7**.[33]

$$Csp = \frac{\int i\,(V)dV}{mV\vartheta} \quad (7.7)$$

Where '*m*' is the mass of active material in the electrode (g), '*V'* is the potential window (V) and 'ϑ' is the scan rate (mV/s).

The specific capacitances of NiC_2O_4 .$2H_2O$ QDs and anhydrous NiC_2O_4 QDs were calculated to be 652 F/g and 1075F/g respectively at 1mV/s. **Figure 7.11 (c)** shows a comparative CV curve nature of NiC_2O_4 .$2H_2O$ QDs and NiC_2O_4 QDs at a scan rate of 30mV/s. From the CV curves, It is visible that the charge storage in NiC_2O_4 ODs is more diffusion-controlled redox compared to more surface-controlled redox in the case of $NiC_2O_4.2H_2O$ ODs.[14-15] At higher scan rates, anodic peak, and cathodic peak potential shifted to more positive, and anodic peak shifted to more negative positions.

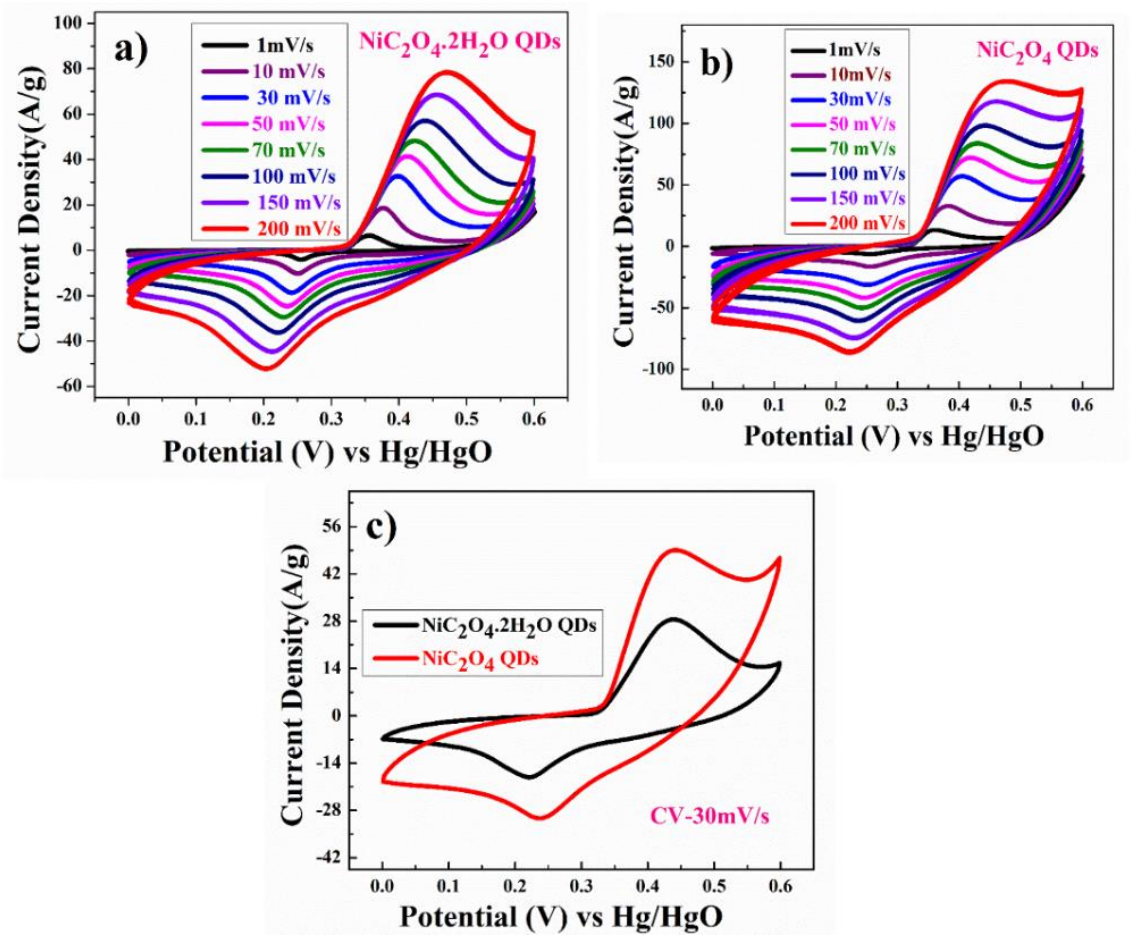

Figure 7.11 (a) Cyclic voltammetry of NiC_2O_4 .$2H_2O$ QDs (b) cyclic voltammetry of anhydrous NiC_2O_4 QDs (c) comparative cyclic voltammetry of NiC_2O_4 .$2H_2O$ QDs and NiC_2O_4 .$2H_2O$ QDs at 10mV/s

7.3.11 Determination of Diffusion coefficient

Figure 7.12 shows the linear relation between anodic and cathodic peak current concerning the square root of scan rate. It confirms that NiC_2O_4 QDs exhibit a more semi-infinite diffusion-controlled process than NiC_2O_4.$2H_2O$ QDs. Furthermore, the electrode kinetics of electrode can be understood by determining the diffusion coefficient. The diffusion coefficient for the electrode was determined using Randles-Sevick eqn.[34]

$$i_p = 2.686 \times 10^5 \times n^{3/2} A D^{1/2} C_o v^{1/2} \quad (7.8)$$

Where i_p is peak current (A), n is the number of electrons transferred in the redox event (usually 1), A is electrode area in cm^2, D is diffusion coefficient in cm^2/s, C_o is OH^- ion concentration in mol/cm^3, v is the scan rate in V/s. OH^- the diffusion

coefficient $NiC_2O_4.2H_2O$ QDs and anhydrous NiC_2O_4 QDs are found to be 1.276×10^{-8} cm^2/s and $5.243\times10^{-8}cm^2/s$.

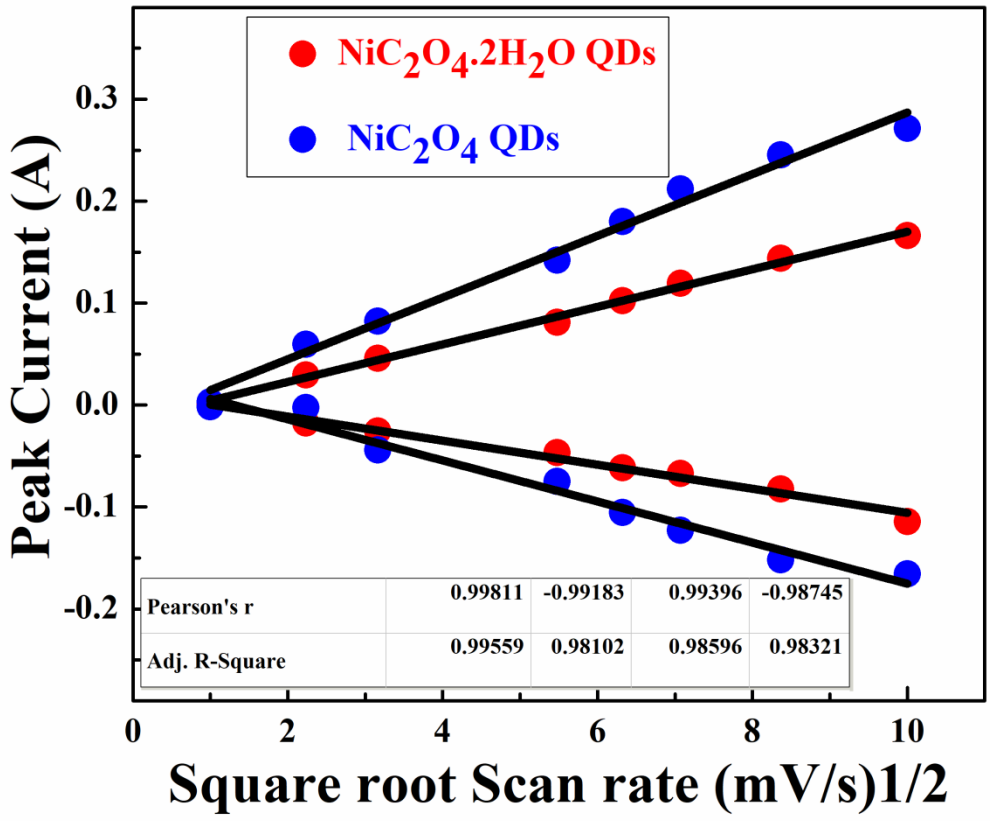

Figure 7.12 Plot of log(peak current vs square root of scan rate of $NiC_2O_4.2H_2O$ QDs and NiC_2O_4 QDs

7.3.12 Determination of b values and analysis

To further understand the electrochemical kinetics of the charge storage performance of the $NiC_2O_4.2H_2O$ QDs and anhydrous NiC_2O_4 QDs electrodes, a power-law equation has been used. The amount of capacitive contribution (surface and diffusion control) for each redox peak was analyzed quantitatively using the CV curves at different scan rates using the power-law represented by **equation 7.9**.

$$i = a\nu^b \tag{7.9}$$

Where *a* and *b* are adjustable values, *i* is the current (A), and ν is the scan rate (V/s). The value of b lies between 0.5 to 1, b= 0.5 stands for the semi-infinite diffusion control reaction i.e. battery-type material, while b = 1 stands for the surface control reaction.[35]

The b values for $NiC_2O_4.2H_2O$ QDs and anhydrous NiC_2O_4 QDs electrodes were calculated at the redox potential of anodic and cathodic peak potential and presented in **Figure 7.13 (**Supporting information**).** b values of $NiC_2O_4.2H_2O$ QDs were found to be 0.609 (at cathodic peak potential) and 0.588 (at anodic peak potential). In the case of anhydrous NiC_2O_4 QDs, the b value was found to be 0.533 (at cathodic peak potential) and 0.513 (at anodic peak potential). b values of both $NiC_2O_4.2H_2O$ QDs and anhydrous NiC_2O_4 QDs clearly explain that charge capacitance at both electrodes is more diffusion-controlled than surface controlled. [14-15]

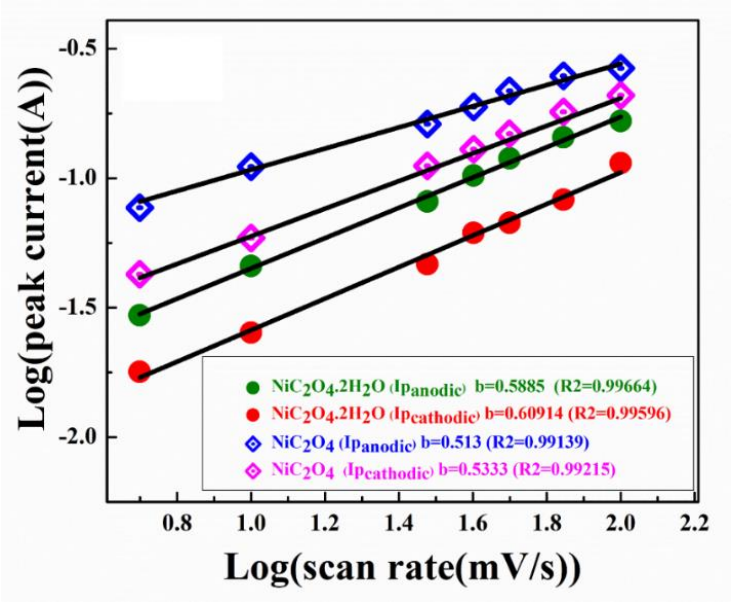

Figure 7.13 b value of Plot of the linear relationship between log (peak current) and log (scan rate) of $NiC_2O_4.2H_2O$ QDs and NiC_2O_4 QDs

7.2.13 Dunn's plot analysis

Voltammetry sweep rate dependence can distinguish quantitatively the capacitive contribution to the current response. The current response at a fixed potential as being the combination of two separate mechanisms, surface capacitive effects, and diffusion-controlled insertion.

$$i(v) = k_1 v + k_2 v^{\frac{1}{2}} \qquad (7.10)$$

Voltammetry sweep rate dependence can distinguish quantitatively the capacitive contribution to the current response. The current response at a fixed potential as being

the combination of two separate mechanisms, surface capacitive effects, and diffusion-controlled insertion. [36]

$$i(\upsilon) = k_1 v + k_2 v^{\frac{1}{2}} \tag{7.11}$$

For more understanding **equation .7.11)** was modified

$$\frac{i(\upsilon)}{\upsilon^{\frac{1}{2}}} = \frac{k_1}{\upsilon^{\frac{1}{2}}} + k_2 \tag{7.12}$$

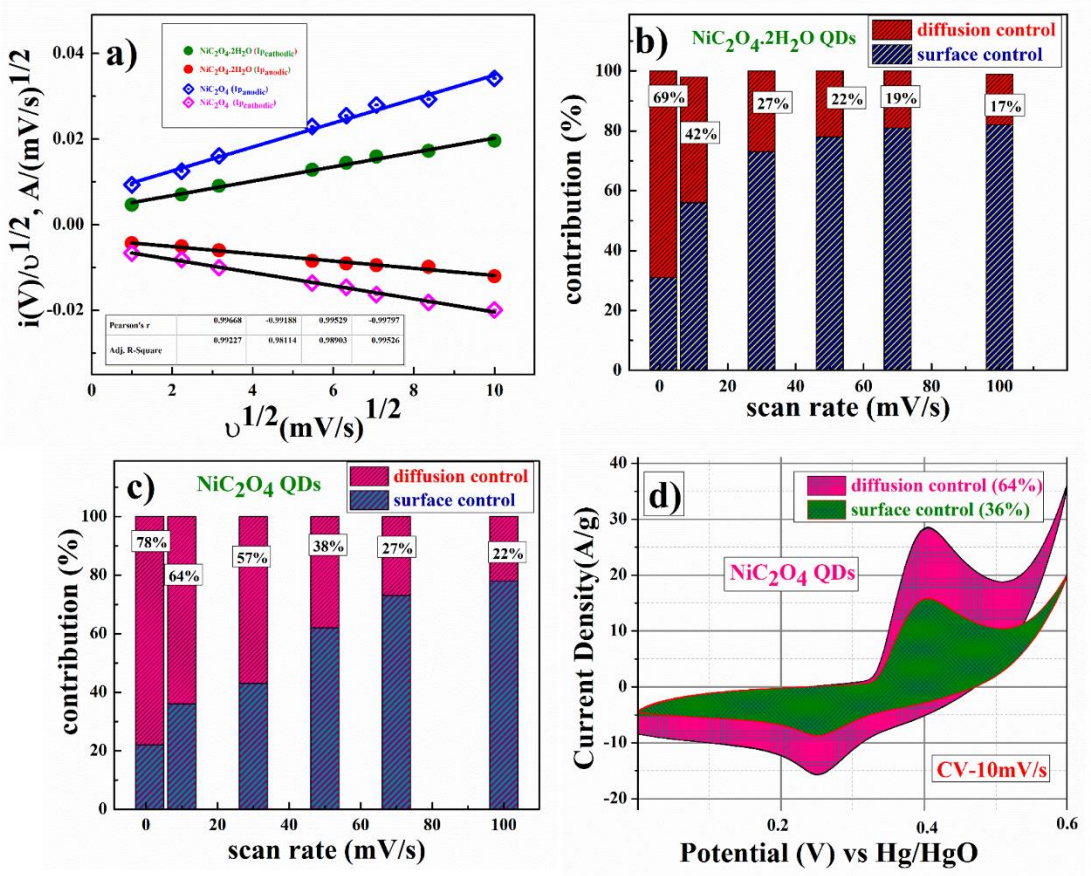

Figure 7.14 (a Contribution of diffusive and capacitive at different scan rates contribution of NiC_2O_4 QDs (b) Analysis of kinetic contribution at 10 mV s−1 of NiC_2O_4 QDs

From **equation (7.9)** $k_1 \upsilon$ and $k_2 \upsilon^{1/2}$ explain the current contributions from the surface capacitive effects and the diffusion-controlled intercalation process, respectively. Thus after the determination of k_1 and k_2, it can be able to quantify, at specific potentials, the fraction of the current due to each of these contributions After done Linear fitted k_1 and k_2 are determined from the slope and intercept of the y-axis.

The representative curve of $i(V)/\upsilon^{1/2}$ vs. $\upsilon^{1/2}$ is in **Figure 7.14 (a-b)** Represents the contribution of surface capacitance and diffusion-controlled interaction with different scan rates of anhydrous NiC_2O_4 QDs, 78% diffusion control, and 22% surface control where $NiC_2O_4.2H_2O$ QDs show 69% diffusion control and 29% surface control in **Figure 7.14 (c)** In **figure7.14 (d)** after determination k1 and k2 value, here represent the contribution of diffusion-controlled interaction (64%) and surface capacitance (36 %) and at peak potential in 0.406V at scan rate10mV/s of anhydrous NiC_2O_4 QDs

7.3.14 Trassati's plot analysis

According to Trassati, the total specific capacitance is the sum of the inner and outer surface capacitance of the electrode and it can be represented by **equation 7.13**.

$$C_{total}=C_{in} + C_{out}\ (F/g)\ldots\ldots \quad (7.13)$$

The specific capacitance contributed from the inner and outer surface of the electrode is dependent upon the scan rate. [37-38] The y-intercept of the linear fit of 1/q vs. $\upsilon^{1/2}$ plot at $\upsilon=0$, represents the total amount of charge stored in the electrode The y-intercept of the linear C vs. $\upsilon^{-1/2}$ at ∞ a represents the outer capacitance stored on the electrode. **Figure. 7.14 (b)** represents the contribution of surface capacitance and diffusion-controlled intercalation at different scan rates. In the case of anhydrous NiC_2O_4 QDs, the contribution of the diffusion-controlled intercalation process was 78% and the contribution of the surface-controlled process was 22% at the scan rate of 1 mV/s. In the case of $NiC_2O_4.2H_2O$ QDs, diffusion-controlled process contribution was 69% and surface-controlled process contribution was 29% at the scan rate of 1 mV/s (**Figure7.14 (c)**. F**igure 7.14 (b)** represent the plot of the contribution of diffusion-controlled intercalation (64%) and surface-controlled capacitance (36 %) at peak potential (0.406V) and scan rate10 mV/s. **Figure 7.15 (a)** presents the y-intercept of the linear fit C^{-1} vs. $\upsilon^{1/2}$ plot. **T**he y-intercept of the linear fit q vs. $\upsilon^{-1/2}$ plot shown in **Figure 7.15 (b)** $\upsilon=\infty$ corresponds to the amount of charge stored at the outer surface of the electrode. After calculating the y-intercept value applied on the Trassati lot, the total capacitance value C_{total} was found to be 1075F/g, in which C_{in} was found to be 771 F/g (72% of total capacitance value), and C_{out} was found to be 304 F/g (28%of total capacitance value).

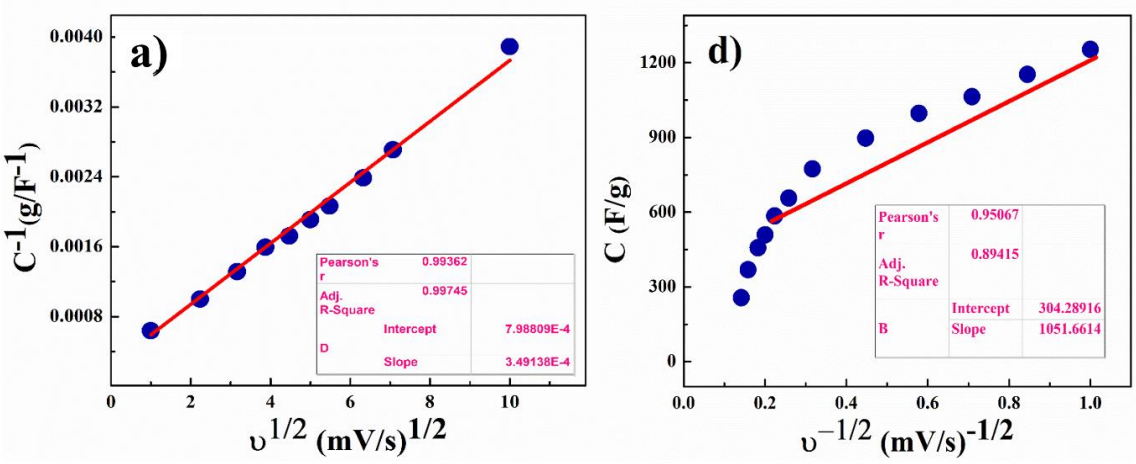

Figure 7. 15 (a-b) Corresponding to Trasatti's plot of NiC_2O_4 QDs

7.3.15 Chonopotentiometry Charge -discharge analysis

Galvanostatic charge/discharge experiments were performed for a more accurate capacitance assessment of $NiC_2O_4 .2H_2O$ QDs and anhydrous NiC_2O_4 QDs electrode samples. From the charge-discharge curve, the specific capacitance of the electrode can be calculated using **equation 7.14**.[39]

$$Csp = \frac{I\Delta t}{m\Delta V} \qquad (7.14)$$

Where I is the discharge current (A), Δt the discharge time (s), m is the mass of the active material in the electrode (g), and ΔV is the potential change during discharge (V). **Figure 7.16 (a)** represents a comparative charge/discharge plot of $NiC_2O_4 .2H_2O$ QDs and anhydrous NiC_2O_4 QDs at a constant current of 1A/g. $NiC_2O_4 .2H_2O$ QDs showed a capacitance equivalent to 1150 F/g and anhydrous NiC_2O_4 QDs showed specific capacitance equivalent to 1638F/g at constant current 1A/g. **Figure 7.16 (b)** Shows the charge-discharge curve at a variable constant current of $NiC_2O_4 .2H_2O$ QDs

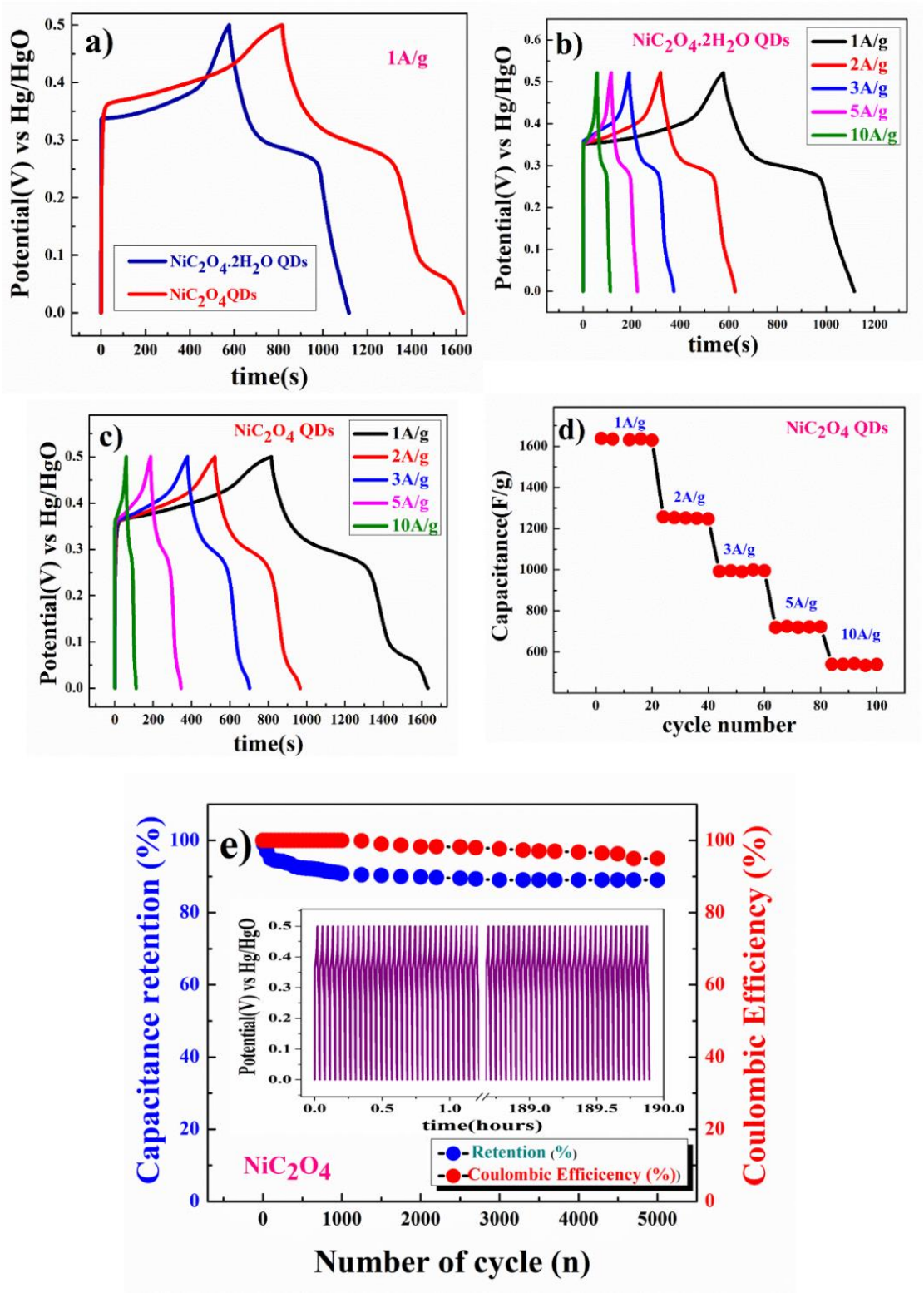

Figure 7.16. (a) the comparative charge-discharge curve at 1A/g of NiC_2O_4 $2H_2O$ QDs and NiC_2O_4 QDs (b-c) charge-charge curve of NiC_2O_4 $2H_2O$ QDs and NiC_2O_4 QDs respectively (d) capacitance performance of NiC_2O_4 QDs at different constant current rates (e) capacitance retention and coulombic efficiency of porous NiC_2O_4 QDs

Figure 7.16 (c) shows the charge-discharge curve at a variable constant current for NiC_2O_4 QDs charge-discharge at a variable constant current. **Figure 7.16 (d)** shows the capacitance value of anhydrous NiC_2O_4 QDs vs cycle number plot at different constant currents. **Figure 7.16 (e)** Exhibits excellent long-term cycle stability of highly porous anhydrous NiC_2O_4 QDs electrodes at 10A/g for 5000 cycles. It was observed that 88% of material retention indicates higher specific capacitance retention after 5000cycles of charge-discharge. Simultaneously, also display the coulombic efficiency ($\eta = {}^{t_d}/_{t_c}$) of the electrode was 95.3 % after 5000cycle of charge/discharge which reveals the high reversibility of the anhydrous NiC_2O_4 QDs electrode.

7.3.16 Electrochemical impedance spectroscopy (EIS) analysis

Figure 7.17 represent the impedance Plot at 10mV, in the frequency range (1MHz-0.1Hz) for $NiC_2O_4.2H_2O$ QDs and anhydrous NiC_2O_4 QDs electrodes. The specific impedance contribution is mainly attributed to electric series resistance (Rs), charge transfer resistance (Rct), and Warburg impedance (Rw).

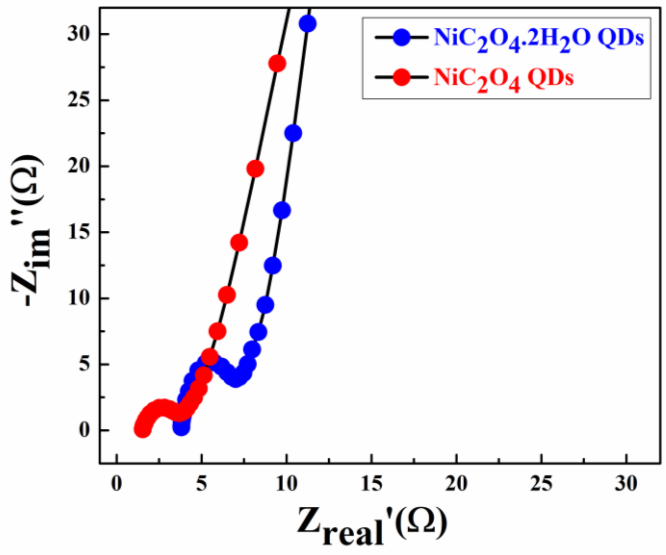

Figure 7.17 EIS plot of $NiC_2O_4.2H_2O$ and porous NiC_2O_4 QDs at 10mV (AC)

The intercept of the EIS spectra of $NiC_2O_4.2H_2O$ QDs and anhydrous NiC_2O_4 QDs on the real axis was at 3.84 Ω, 1.28 Ω indicating very small internal resistance of the electrodes. The small semicircle in the high-frequency region shows the fast charge transport between electrode and electrolyte as (Rct) values were only 2.9 Ω, and 3.84

Ω for $NiC_2O_4 .2H_2O$ QDs and anhydrous NiC_2O_4 QDs electrodes respectively. The straight line in the low-frequency region of the anhydrous NiC_2O_4 QDs electrode is close to a 90° angle (very close to –Z″(Ω) axis) from the horizontal line representing the characteristic of more pseudocapacitance behaviour for porous anhydrous NiC_2O_4 QDs electrode. This also represents the fast OH- ion diffusion in the porous electrode structure. [40]

7.3.17 Full cell cyclic voltammetry (CV) of Activated carbon // of $NiC_2O_4 .2H_2O$ QDs and NiC_2O_4 QDs in 2M KOH analysis

To understand the real charge storage behaviour of anhydrous NiC_2O_4 QDs sample relative to AC(Activated carbon), two electrode measurements have been conducted in 2M KOH. To determine the maximum specific capacitance during the full test, the storage capacity of positive and negative electrodes need to be balanced as per the following equation:

$$\frac{1}{C_{total}} = \frac{1}{C_{positive}} + \frac{1}{C_{negative}} \quad (7.15)$$

For balancing the charge storage capacity of the cell, the mass ratio (m^+/m^-) of positive and negative electrode material was measured using the following equation:

$$\frac{m^+}{m^-} = \frac{C_- \times \Delta E_-}{C_+ \times \Delta E_+} \quad (7.16)$$

$m^+, m^-, C_+, C_-, \Delta E_+, \Delta E_-$ are mass, specific capacitance, and potential window of positive and negative electrodes estimated by three-electrode measurement.[41-42]

Figure 7.18. (a) Shows compare the CV curve at a 10 mV/s scan rate in 2M KOH electrolyte where $NiC_2O_4 .2H_2O$ QDs and anhydrous NiC_2O_4 QDs positive electrodes and where used AC (activate carbon) is the negative electrode. The calculated mass ratios ($\frac{m^+}{m^-}$) were 1:3.1 and 1:4.24 for the asymmetric cell of $NiC_2O_4 .2H_2O$ QDs and anhydrous NiC_2O_4 QDs simultaneously. **Figure 7.18. (b)** Demonstrates the comparative CV at 10mV/s curve in 2M KOH where $NiC_2O_4 .2H_2O$ QDs and anhydrous NiC_2O_4 QDs vs. AC two-electrode ASCs (Asymmetry Supercapacitors) **Figure 7.18. (c-d)** shows full cell CV from 1mV/s to 100mV/s in this potential window (1.6V) of $NiC_2O_4 .2H_2O$ QDs and NiC_2O_4 QDs //AC two-electrode ASCs

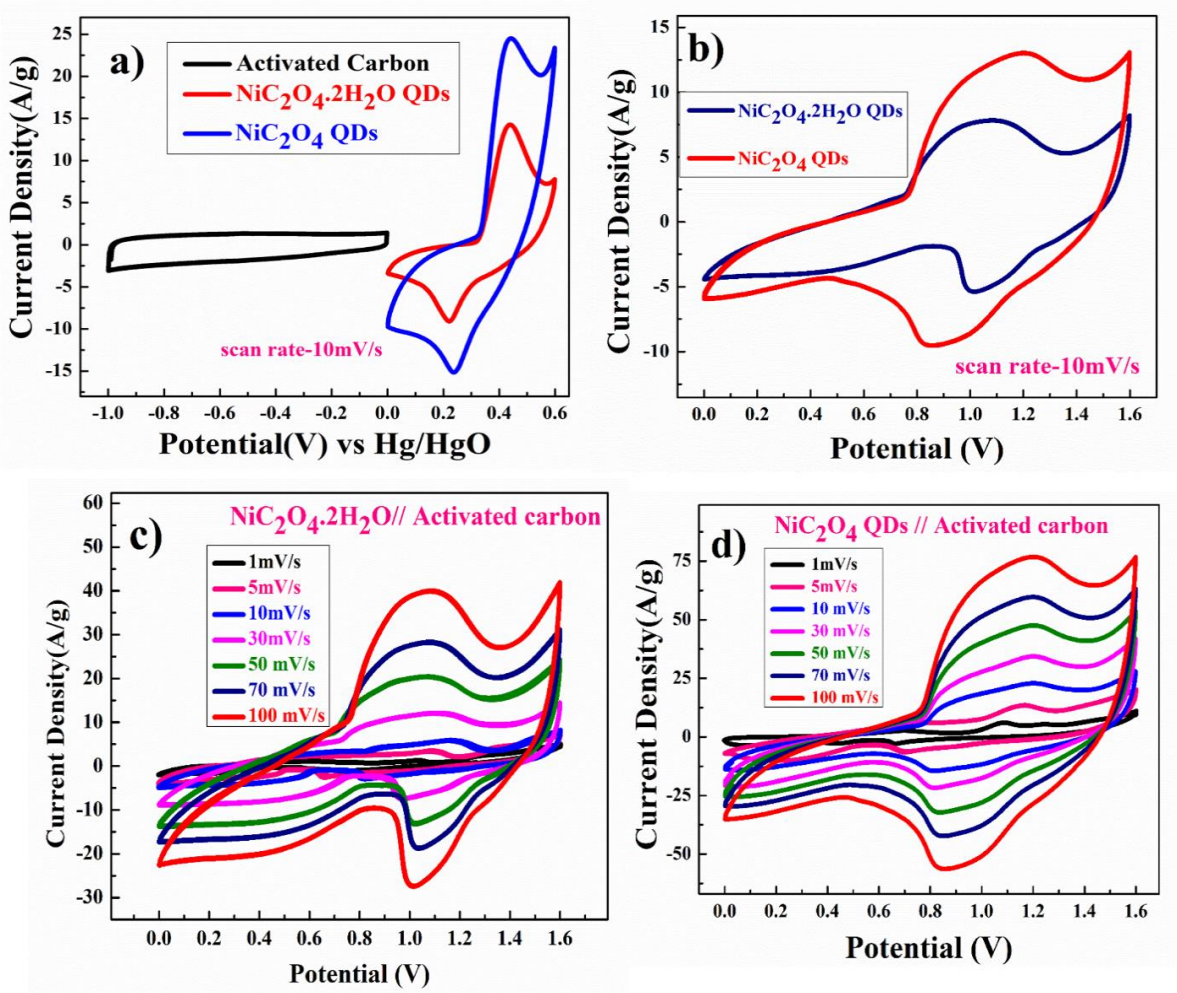

Figure. 7.18 plot for activated carbon and non-hydrate NiC_2O_4 QDs cell in ASC mode (a) Compare single electrode CV of Activated Carbon vs.NiC_2O_4 $2H_2O$ QDs and NiC_2O_4 QDs at 10 mV/s, in 2M KOH (b) compare Full cell CV both NiC_2O_4 .$2H_2O$ QDs and NiC2O4 QDs at 10 mV/s scan rates in 2M KOH, (c-d) Full cell CV of NiC_2O_4 .$2H_2O$ and NiC_2O_4 QDs at different scan rate charge-discharge in 2M KOH respectively

7.3.18 Full cell charge-discharge of Activated carbon // NiC_2O_4 .$2H_2O$ QDs and NiC_2O_4 QDs in 2M KOH analysis and stability of AC// NiC_2O_4 QDs after 2500 cycles

Figure 7.19 (a) Comparative full cell charge-discharge at 1 A/g in 2 M KOH, where NiC_2O_4 .$2H_2O$ QDs show 556 F/g and NiC_2O_4 QDs 826 F/g subsequently capacitance values were calculated by **equation 7.14**, **Figure 7.18. (b)** Shows charge/discharge conducted for measuring the actual capacitance, capacitance values are 826 F/g, 676 F/g, 631 F/g, 484 F/g, and 232 F/g at current density, i.e.,1 A/g, 2 A/g, 3 A/g, 5 A/g,

and 10 A/g respectively. **Figure 7.18 (d)** Shows coulombic efficiency of a two-electrode cell has lost only 3% and higher capacity retention of 89.4% of its initial value after 2500cycles.

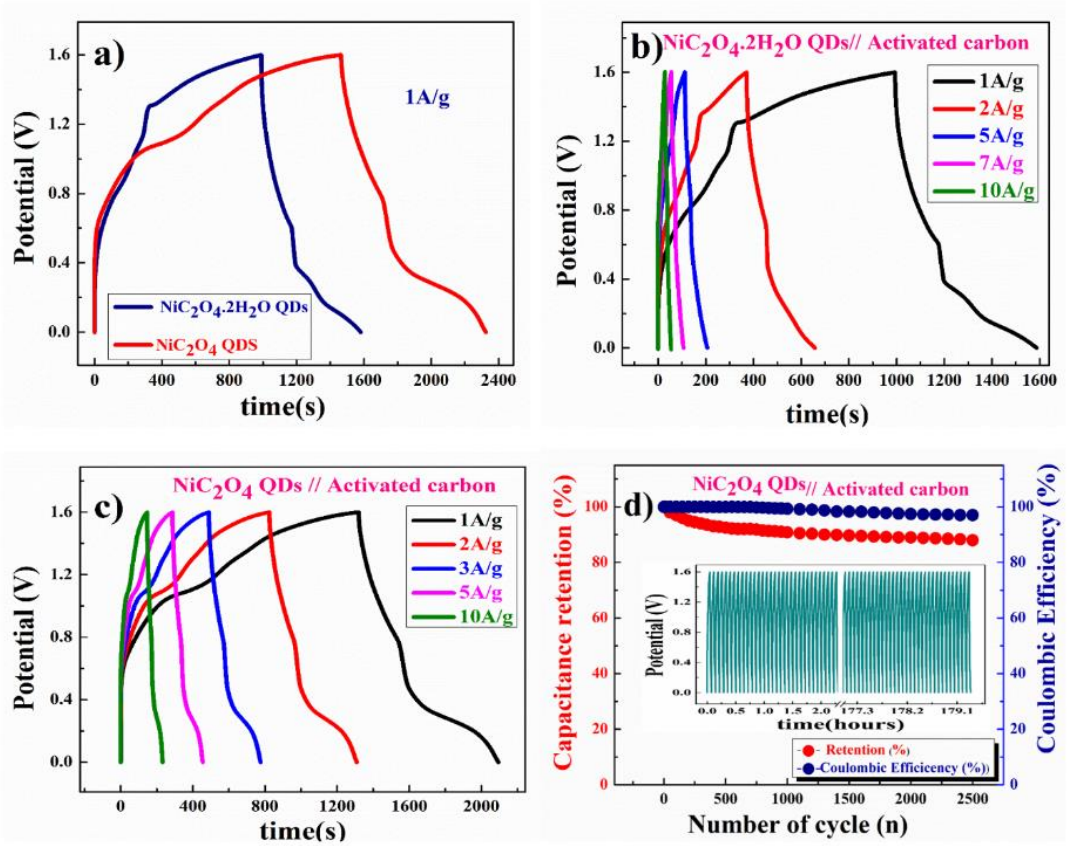

Figure. 7.19 (a) compare Full cell charge-discharge of both NiC_2O_4 $2H_2O$ QDs and NiC2O4 QDs at 1A/g in 2M KOH (b-c) Full cell charge-discharge of both NiC_2O_4 $2H_2O$ QDs NiC_2O_4 QDs at a different constant current in 2M respectively (d) Capacitance retention and coulombic efficiency of NiC2O4 QDs in 2M KOH

7.3.19 Comparative Electrochemical impedance spectroscopy (EIS) analysis Activated carbon // of $NiC_2O_4.2H_2O$ QDs and NiC_2O_4 QDs in 2M KOH analysis

Figure 7.20 shows the comparative EIS (Nyquist) plot for $NiC_2O_4.2H_2O$ QDs and anhydrous NiC_2O_4 QDs electrodes in full cell ASCs mode in the frequency range (1MHz to 0.1Hz) at 10mV applied potential. Superior diffusion behaviour in the low-frequency region and higher charge transfer in the high-frequency region was observed for anhydrous NiC_2O_4 QDs

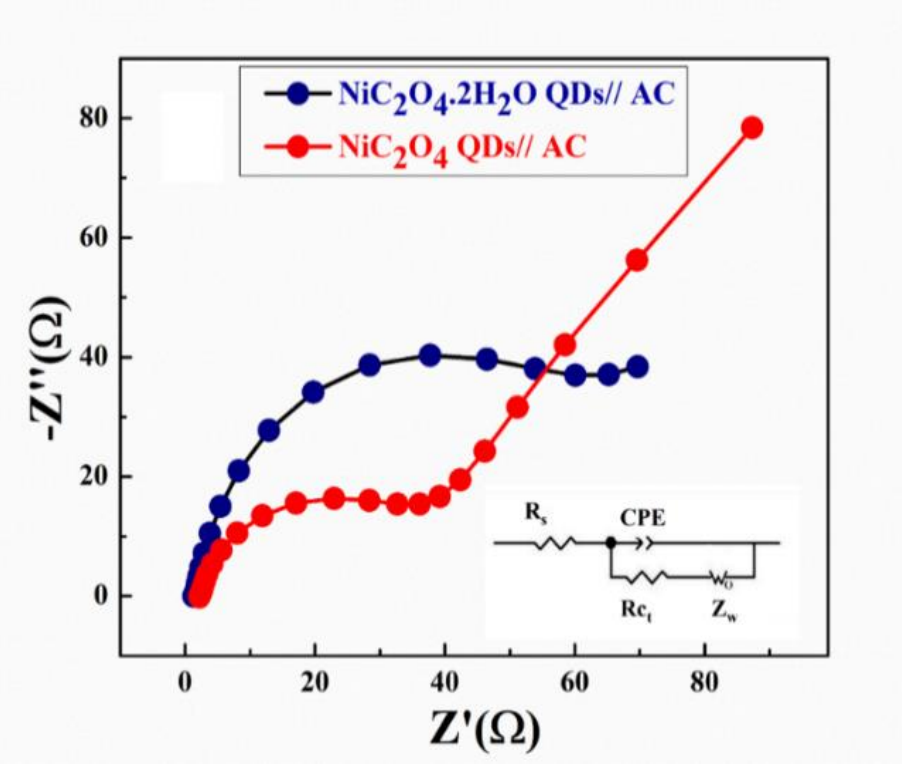

Figure 7.20 shows a comparative EIS plot (Nyquist) of NiC_2O_4 .$2H_2O$ QDs and anhydrous NiC_2O_4 QDs in the frequency range (1MHz to 0.1Hz) at 10mV/s shows, that anhydrous NiC_2O_4 QDs has higher charge transformation and higher diffusion \

.lbehaviour in the low-frequency region

7.3.20 NiC_2O_4 QDs electrochemical analysis in 1M Na_2SO_4

Figure 7.21 (a) Shows the CV curve of anhydrous NiC_2O_4 QDs in 1M Na_2SO_4 and operating voltage window0.7V, **Figure 7.20 (b)** represents the charge-discharge of NiC_2O_4 QDs, after calculating specific capacitance in 1M Na_2SO_4 is 546F/g **Figure 7.20 (c)** comparative EIS plot (Nyquist) of $NiC_2O_4.2H_2O$ QDs and anhydrous NiC_2O_4 QDs in the frequency range (1 MHz to 0.1 Hz) at 10mV/s in 1 M Na2SO4

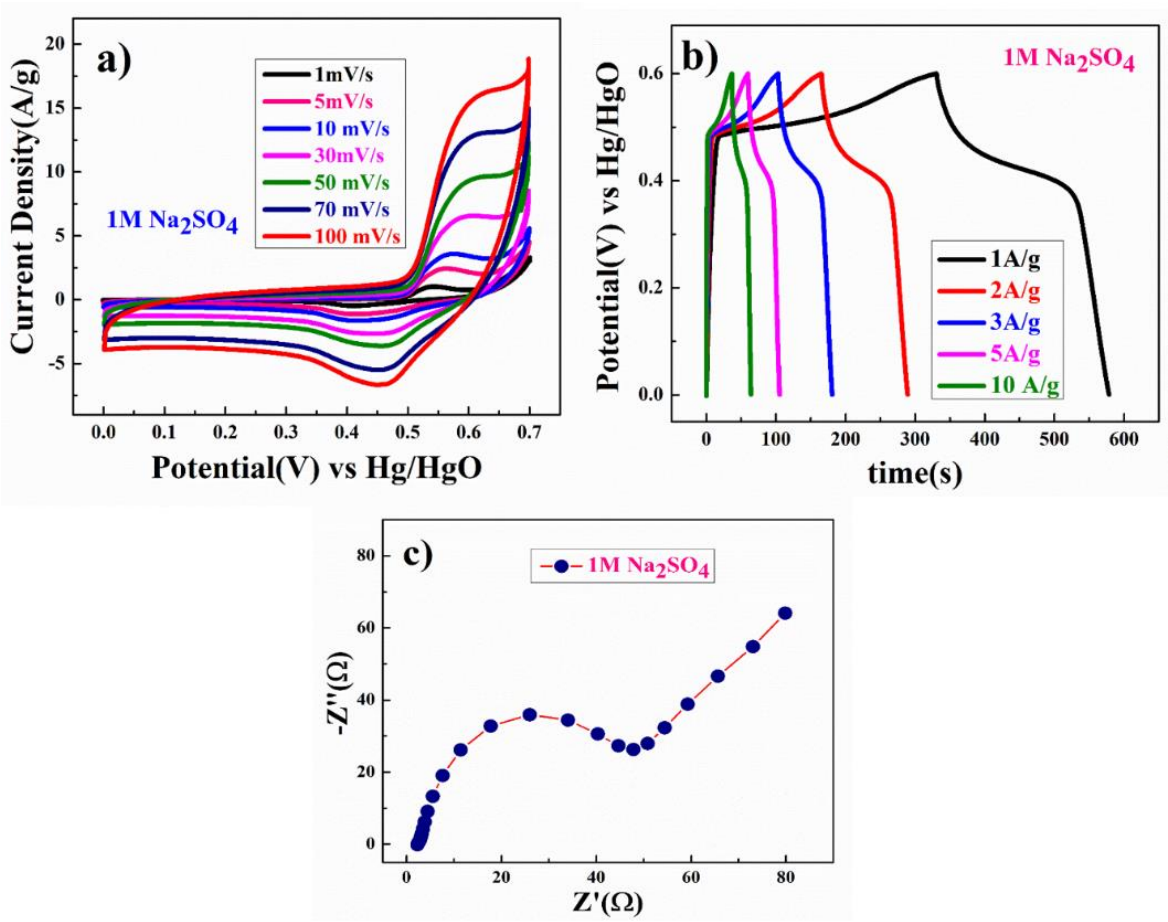

Figure 7.21 (a) compare Full cell charge-discharge of both NiC_2O_4 $2H_2O$ QDs and NiC2O4 QDs at 1A/g (b) compare Full cell charge-discharge of NiC_2O_4 QDs at different constant current (c) EIS both NiC_2O_4 $2H_2O$ QDs and NiC2O4 QDs at 10 mV(AC)

7.3.21 Full cell AC// NiC_2O_4 QDs electrochemical analysis in 1M Na_2SO_4

Figure 7.22. (a) Shows full cell CV curve of anhydrous NiC_2O_4 QDs Vs. Activated carbon in 1M Na_2SO_4 in voltage windows 1.6V **Figure 7.22 (b)** Corresponding charge-discharge of full cell NiC_2O_4 QDs vs. AC, **Figure 7.22 (c)** shows an EIS plot (Nyquist) of anhydrous NiC_2O_4 QDs in the frequency range (1MHz to 0.1Hz) at 10mV/s in 1 M Na_2SO_4. **7.22. (d)** shows coulombic efficiency of a two-electrode cell has lost less than 2% and higher capacity retention of 93% of its initial value after 2000cycles

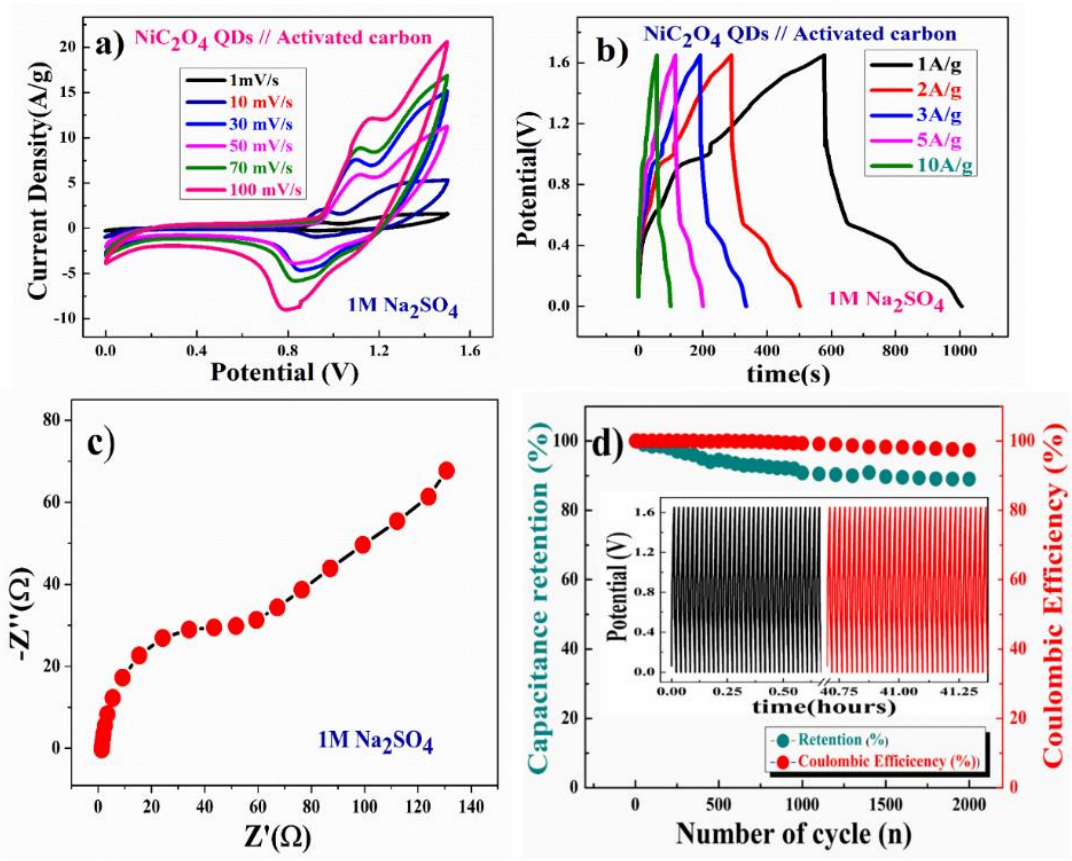

Figure. 7.22 (a) Full cell CV NiC_2O_4 QDs // Activated Carbo in 1M Na_2SO_4 (b) Full cell charge-discharge of NiC_2O_4 QDs in 1M Na_2SO_4 at different constant current (c) EIS both $NiC_2O_4.2H_2O$ QDs and NiC_2O_4 QDs at 10 mV(AC) (d) Capacitance retention and coulombic efficiency of NiC_2O_4 QDs

7.3.22 Comparative Power Density vs Energy Density of AC// NiC_2O_4 QDs in 2M KOH and 1M Na_2SO_4

Specific energy and specific power of asymmetric capacitors were calculated using the following equations:

$$E(Wh/kg) = \frac{1}{2}\frac{C_{ASCs}}{3.6}V^2 \quad (7.17)$$

$$P(W/kg) = \frac{E*3600}{t_{dis}} \quad (7.18)$$ Where

C_{ASCs} is specific capacitance, V is operating voltage and t_{dis} is discharge time. [43]

Figure 7.23 shows a plot of specific energy vs. specific power with a different constant current of anhydrous NiC_2O_4 QDs Vs. Activated carbon in 1M Na2SO4 and 2M KOH in voltage windows 1.6V. The highest specific energy of 126 Wh/kg and specific power of ~480W/kg at 1 A/g current density in 1M Na2SO4 and The resultant values are the highest specific energy of 293 Wh/kg and specific power of ~772W/kg at 1 A/g current density. Maximum specific power of ~2844W/kg was obtained when specific energy was reduced to ~87 Wh/kg at 10 A/g of current density in 2M KOH

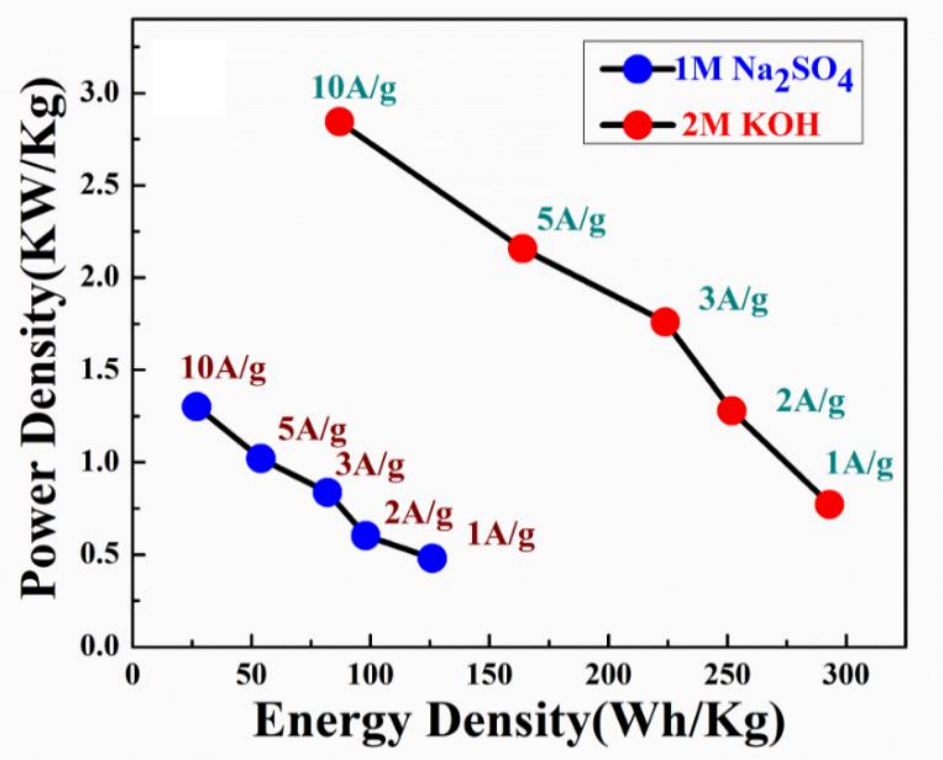

Figure 7.23 Ragone plot (Energy density vs power density) of NiC_2O_4 QDs in 2M KOH and 1M Na_2SO_4

7.4 Conclusions:

In summary anhydrous NiC_2O_4QDs were successfully synthesized using a two-step process, first $NiC_2O_4 .2H_2O$ QDs were synthesized by the colloidal suspension with a control precipitation method in a ratio of 1:1 aqueous and isopropyl alcohol medium then $NiC_2O_4 .2H_2O$QDs were heated 180^oC for 5hrs resultant product was formed as anhydrous NiC_2O_4QDs. It is highly pseudocapacitive in exhibiting a specific capacitance of 1638 F/g at the current density of 1A/g and having excellent cyclic

stability.

Predominant diffusion control over surface control mechanism seems to operate behind high charge storage as intercalative (Inner) and surface (outer) charges stored by porous anhydrous NiC_2O_4 QDs were close to high at 38% and 62% respectively. Anhydrous NiC_2O_4 QDs //AC full cell resulted in 293Wh/kg of maximum specific energy with specific power equivalent to 772W/kg in the voltage window of 1.6V in 2M KOH electrolyte. These results confirm that porous anhydrous $NiCO_4$ QDs can act as a potential pseudo-capacitive electrode for large energy storage applications.